IOP Conf. Series: Journal of Physics: Conf. Series **842** (2017) 012077 doi:10.1088/1742-6596/842/1/012077

Micro CT Analysis of Dynamic Damage in Laminates: Impact *vs*. blast loading

Laurence A Coles, Anish Roy, Vadim V Silberschmidt

Wolfson School of Mechanical, Electrical and Manufacturing Engineering, Loughborough University, Ashby Road, Leicestershire, LE11 3TU, UK

Abstract. Dynamic loading is often an unavoidable condition in various applications of carbon-fibre-reinforced polymers and can cause various modes of damage. Realisation of dynamic damage in composites can differ significantly from that under quasi-static loading conditions. A comprehensive study of damage in composites caused by a wide variety of impact and blast loading is currently lacking. The work presents a detailed analysis of damage in specimens of a 2×2 twill weave T300 carbon-fibre/epoxy composite subjected to ballistic loading with both steel and ice projectiles (with energies from 95 J to 865 J at 70-90 m/s and 300-500 m/s, respectively) and air blast (with incident pressures of 0.4 MPa, 0.6 MPa and 0.8 MPa and wave speeds between 650 m/s and 950 m/s). The resultant damage was analysed in-depth based on detailed volumetric data obtained with high-resolution X-ray micro computed tomography.

1. Introduction

Over the last few decades the use of fibre-reinforced composites (FRCs) has risen considerably across many areas of application including automotive, aerospace, naval, defence, energy and sport. Service conditions of all these areas can include dynamic loading events, resulting in minor or major damage to components or structures. Some examples of typical dynamic loading may include: low- and high-velocity impacts (1 to 1000 m/s) ranging from flight at Mach 1-2 (300-600 m/s) of fast jets or intercontinental ballistic missiles through clouds of airborne debris or hailstone, to lower-velocity events caused by debris on runways, railway lines, automotive race tracks etc., or even air-blast loading such as interaction with close-proximity explosions or sudden increases in local pressure. As a result, it becomes increasingly important to understand fully the effect of various dynamic loading conditions on a FRC's response, in terms of both local and global deformation as well as visible and hidden damage.

The last decade has seen a vast amount of research effort towards characterising the response of FRCs to various dynamic loading conditions [1], but drawing comparisons between these studies is challenging and often impossible due to their major differences such as type of specimens and, more importantly, experimental and analytical methodologies. In the past, some papers tried to surmise an overview of, for example, impact behaviour [2, 3] and [4, 5], but given a breadth of experimental data drew mostly qualitative conclusions regarding the effects of differences in methodology, specimen as well as projectile mass and velocity on such features as delamination behaviour.

An important aspect of this dynamic study is understanding the types of loading conditions and

their effect on the specimen over time. For instance, a large part of both ballistic experimental and numerical studies was focused on the resulting deformation and damage caused by solid (typically steel) projectiles. In recent years, efforts were made to understand the impact process of ice projectiles [6-8], the blast response of composites [9-11] and the effect on composite specimens as well as distribution of load and dispersion of kinetic energy. But, typically, the analysis of the induced damage is limited to a visual inspection of external surfaces, or a use of invasive techniques to study internal damage; the latter could introduce unwanted damage complicating the analysis [12-16]. Still, some studies employed X-ray tomography to investigate damage [17].

This paper presents the experimental case studies of both ballistic impact with steel and ice projectiles and air blast loading of carbon fibre/epoxy specimens, using digital image correlation and X-ray computed tomography (CT) to investigate and compare the levels of deformation and damage.

2. Experimental Setups

2.1. Materials and Specimens

The tested carbon-fibre-reinforced/epoxy specimens, measuring approximately 195 mm x 195 mm with a thickness of 5.6 mm (SD = 0.031mm) were fabricated from 10 plies of carbon-fibre fabric, pre-impregnated with a toughened epoxy matrix (IMP530R). The 10 plies were formed to a laminate consisting of two surface plies (T300 3K fibres) and eight central bulking plies (T300 12K fibres), with a 2 × 2 twill weave 0°/90° layup configuration and with a theoretical density of 1600 kg/m^3. All specimens were manufacture using the autoclave process as a flat sheet, cured at 120°C with a 1.5°C per minute ramp rate and a soak time of 160 minutes at a pressure of 90 psi under full vacuum.

2.2. Pneumatic Gun Setup

The investigation was performed on a specially developed ballistic experimental apparatus utilising a pneumatic gun. The CFRP specimens were installed into a 4-axis positioning system, and aligned with the barrel resulting in a cantilever clamping scheme, with all specimens being subjected to a orthogonal impact (as shown in Figure 1). The projectile was accelerated to the required speed in the barrel using compressed air, and muzzle velocity measurements were collected using a light gate device installed between the specimen and the end of barrel. Projectile velocities were then determined by the time difference between the signal peaks from the light gates; the experiment was controlled by a PC via a PXI system (National Instruments). The impact process was captured using two high-speed cameras (Photron Fastcam SA5) configured in two arrangements, the first of which captured the front and top views at 25,000 - 50,000 frames per second while the second recorded the rear surface for digital image correlation (DIC) using the VIC-3D (Correlated Solutions) system at 60,000 frames per second.

2.3. Shock Tube Setup

In this setup, the specimens were positioned vertically on a three-point-bending style fixture, which consisted of 2 knife edges (slightly rounded) located 152.4 mm apart, the rest of the specimen was unsupported (as shown in Figure 2). A rubber band was used to keep the specimen firmly against the knife edges, while positioned vertically on the fixture. The shock tube apparatus (8 m in length) consisting of a driver, diaphragm and driven section, produced the air blast shockwave by pressurising the driver section until a critical pressure, at which the diaphragm ruptured creating a dynamic pressure-wave profile. The muzzle of the shock tube, with its inner diameter of 76.2 mm, was moved towards the specimen until there was only a paper thin gap between the specimen and the muzzle (approximately 0.1-0.2 mm). Pressure sensors located towards the end of the muzzle recorded the shockwave profile.

The deformation process was captured using three cameras (Photron SA1 Photron USA, Inc., CA,

USA), two cameras recording at 28,800 fps viewed the rear surface of the specimen for DIC using the VIC-3D (Correlated Solutions) system. A third camera, also recording at 28,800 fps, was placed perpendicular to the edge of the specimen to acquire side-view images and observe the mechanisms of failure for each specimen.

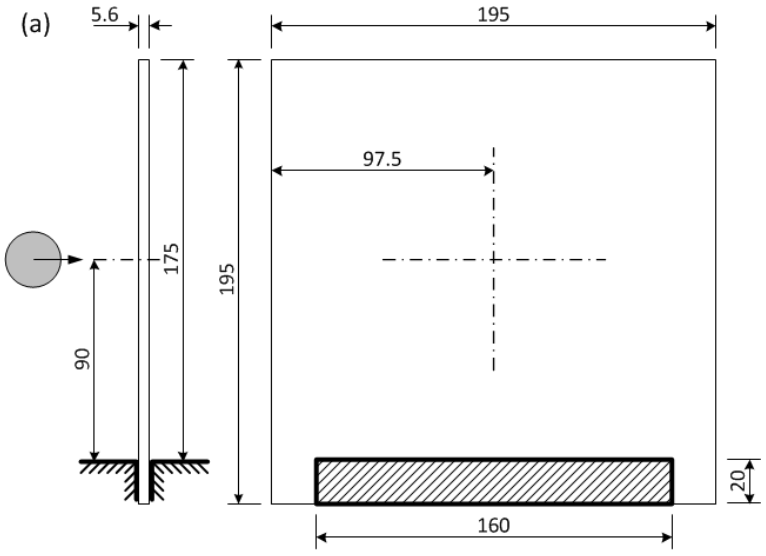

Figure 1. Ballistic impact regime and cantilever clamping fixture

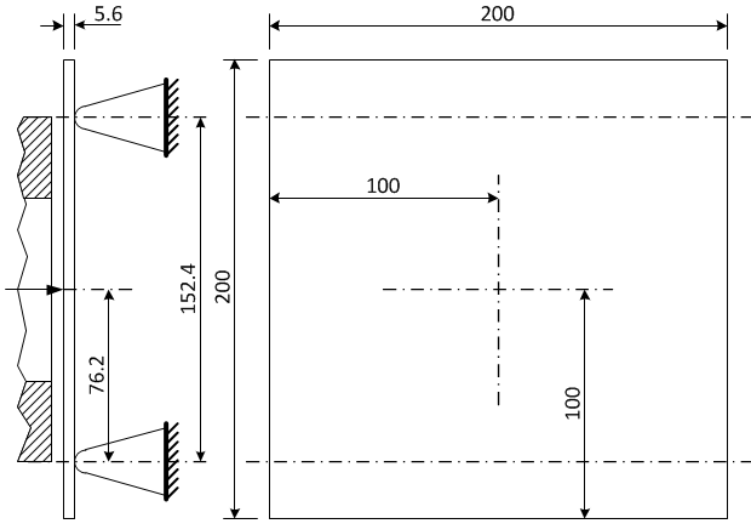

Figure 2. Air blast regime and three-point-bending fixture

2.4. Experimental Parameters

All the solid (steel) projectiles were 23.8 mm diameter with a weight of 54.7 g, and the fragmenting ice (hailstone imitation) projectiles had a diameter 25 mm with a weight of 7.5 g at a temperature of -20°C. The impact velocities for the ballistic and air blast cases were chosen to produce three levels of damage in the specimens – minor, medium and major with penetration, and were determined during calibration experiments to correspond to approximately 60, 75 and 90 m/s for the steel projectiles, 300, 400 and 500 m/s for the ice impacts and incident pressures of 0.4 MPa, 0.6 MPa and 0.8 MPa for the air blasts with respective reflected pressures of 1.35, 2.50 and 3.4 MPa, and had wave speeds of between 650 m/s and 950 m/s. A total of 28 samples were subjected to various loading conditions, 9 to impacts with the solid steel projectiles, 9 to impacts with the ice projectiles and 10 to the air blasts.

2.5. Configuration of X-Ray Tomography Scans

All the specimens were inspected using a Metris 160 H-XT X-ray micro CT system to investigate the extent of the internal damage and its spatial distribution. Each scan was conducted at 140 kV and 130 µA using a tungsten target, with 2650 radiography projections taken over the 360° rotation for each specimen at an exposure of 500 ms. In order to reduce granular noise, 8 images where taken and averaged per projection. The total volume scanned for each specimen was 180 mm x 140 mm x 20 mm at a resolution of 97 µm.

3. Experimental results and discussion

Typical impacts with both the steel and ice projectiles in the experimental studies can be seen in Figure 3, with a characteristic response of the major damage air blast condition shown in figure 4. The ice projectile initially indented the specimen before fragmenting within it, causing major wide-spread delamination of the first few plies. The impact with the steel projectile resulted in major indentation before full penetration, as expected, inducing more localised damage when compared to that of the ice projectiles. And, finally, the specimen subjected to the air blast undergoes global flexural bending between the supports with damage initiating at the centre of the rear surface.

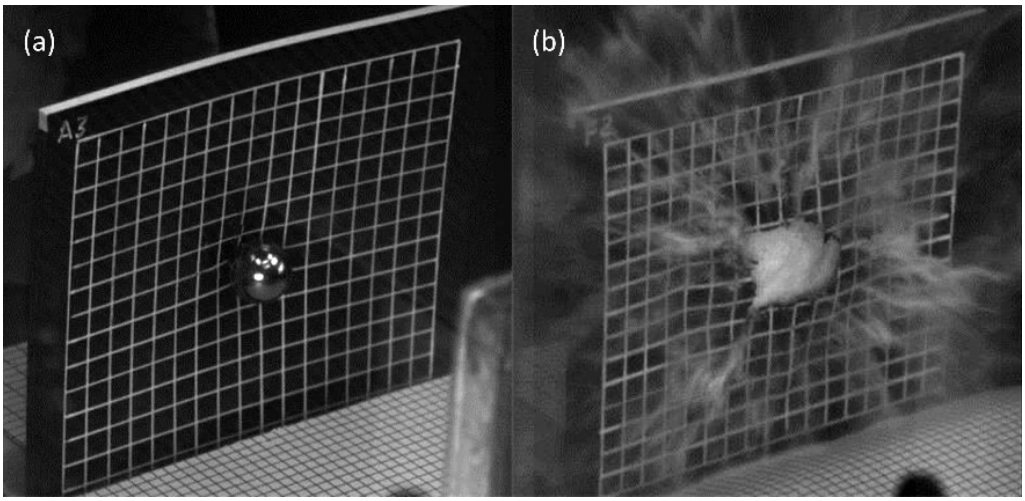

Figure 3. Typical impact behaviour of solid steel projectile at 0.40 ms (a) and fragmenting ice projectile at 0.19 ms (b)

Figure 4. Typical damage in dynamic response to air blast at 0.13 ms

3.1. Deformation Analysis

3.1.1. Ballistic Impact

Analysing impacts with the steel projectile in terms of global displacement, it is clear that due to the more rigid nature of the material, the composite demonstrated more defined indentation before the transition into global flexural bending. For the ice projectiles, this initial indentation was still present, but upon fragmentation, this local indentation was more gradually transitioned due to the distributed load, leading to global bending. This difference in the distribution of dynamic loads led to varying curvature of the specimen during loading. For the solid projectiles, the curvature was small, with transitions between concave and convex forms happening gradually, whereas for the ice projectile this transition was more abrupt and resulted in multiple damage modes. As the ice fragmented on impact,

the local indentation of the specimen became more widespread causing a more distributed loading and, hence, reduced failure at the rear surface. In the case of the solid projectile, this damage occurred much sooner.

From localised deformation behaviour and the normalised response of each specimen, it became evident that the maximum out-of-plane displacement increased with the growing impact velocity (energy). The time until maximum displacement reduced with the increased velocities (energies), although this trend was not as clear due to the limitation related to time resolution (directly linked to the frame rate of the used camera).

3.1.2. Air Blast

Analysis of the centre-point displacement of each specimen demonstrated clearly that they all show an initial oscillation, achieving maximum displacement before the oscillations decayed gradually due to the contact surface behind the shockwave and resultant back pressure. Double and triple peaks were observed on the centre-point displacement oscillations, the former representing the transition of lateral oscillations to the free edges and back again. The triple peaks show similar behaviour, but the centre peak was related to delamination of a given number of plies that were then free to move with higher deflection due to reduced local stiffness. As a result, delamination was initiated at different times for each pressure magnitude, after which both the amplitude and frequency of the oscillations changed due to the expected reduction in specimen stiffness.

Observations of vertical and horizontal out-of-plane displacement line sections demonstrated that the deformation and transitions in curvature of each specimen resulting from the different air-blast magnitudes were similar, with no obvious differences, except from increasing out-of-plane displacement as excepted. Given the widely distributed loading in this case, there is minimal localised indentation, and all specimens undergo global flexural bending. As the air-blast magnitude increased, the specimens see greater deformation of the rear surface at the centre of the free edges. This was caused by the increasing damage and delamination of the rear surface because of increased bending stress. Although this is more apparent for the major damage case, the progression of increased deformation at the free edge increased at each damage level before resulting in a clear failure.

3.2. Damage Analysis

Micro CT inspections of the specimens after ballistic impact tests with the solid (steel) and fragmenting (ice) projectiles demonstrated two very distinct types of visual damage: (i) highly localised and, therefore, more penetrating damage from the steel projectiles and (ii) more widespread damage to the front surface of the specimen with some signs leading to the early stages of penetration in the case of the ice projectiles. Figure 5 shows the damage clouds for two major damage ballistic loading conditions. For the air blast loading, the minor damage case showed no signs of external damage, whereas the medium and major cases resulted in clearly increasing levels of damage at the rear surface as the air blast magnitude increased. The damage across all cases can be compared to that of standard static three-point bending. For this type of composite specimen, the first signs of damage appear along a central line, which is the line of symmetry between the supporting locations, as tensile failure of the individual plies leading to substantial delamination. At the front surface for each specimen there were no signs of any damage until complete failure, suggesting that the tensile failure and resultant damage propagates from the rear surface to the front surface. Figure 6 shows the damage clouds for the major-damage air-blast loading conditions. From the CT scans it is clear that for all cases, the main damage modes were delamination and tensile fibre damage at the rear surface, but at the employed resolution it was not possible to accurately determine any other damage mechanisms.

This was confirmed for all the three damage cases across all loading conditions by means of 3D analysis: for the steel projectile, the damage cloud remained highly localised even under increasing

energy whereas for the ice projectile it increased more clearly. For the air blast cases with increasing intensity, the levels of tensile failure and delamination at the centre and free edges of the specimen grew, transforming the circular loading area into a central symmetrical band of damage.

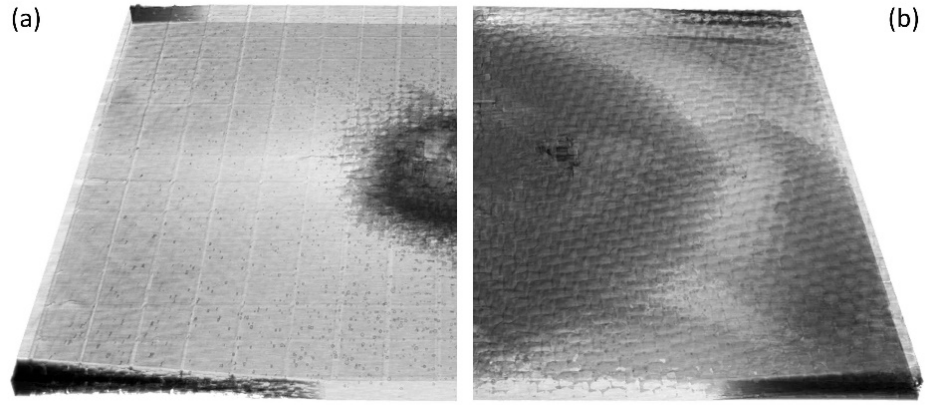

Figure 5. Typical examples of internal damage cloud in composite specimens caused by solid steel (a) and fragmenting ice (b) projectiles (half specimens are shown)

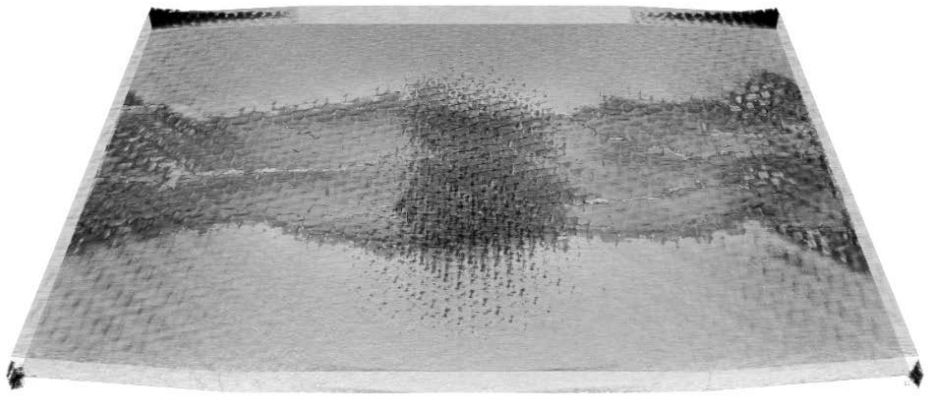

Figure 6. Typical example of internal damage cloud for major damage case

The transparent 3D tomograms shown in Figures 5 and 6 allowed assessment of the damage areas and greyscale intensity, with the latter related to the extent of damage accumulation through the specimen's thickness. For instance, the specimen impacted with the solid projectile demonstrated a dark-grey zone toward the centre, indicating greater damage (like penetration), whereas the fragmenting projectiles caused catastrophic damage across the whole front surface and first few plies of the composite target, causing a more distributed gradient of the intensity. The same can be said for the air-blast loading, where the major-damage case showed the higher intensity at the central area and free edges, i.e. a larger amount of through-thickness damage in these locations.

Observing the 2D horizontal and vertical cross sections of each specimen, it was possible to approximately measure this spread of damage with resolution of 97 μm. Figure 7 shows the final averaged damage areas against the averaged maximum out-of-plane displacement for various loading conditions.

4. Conclusions

For impacts with projectiles of the same size, a case with the solid (steel) projectiles demonstrated more defined indentation of the CFRP specimens before the transition to global flexural bending. In

contrast, the fragmenting (ice) projectiles produced initial indentation that, upon fragmentation, more gradually transitioned to distributed loading leading to global flexural bending. Comparison of dynamic loading conditions showed that projectiles of the same material produced similar responses of the impacted specimen, even at different energy levels. Oppositely, two projectiles of different materials will show different levels of indentation within the specimen, even at lower energy levels. The character of transition from indentation to global flexural bending also changed with the projectile material, affecting the evolution of specimen's curvature during its deformation.

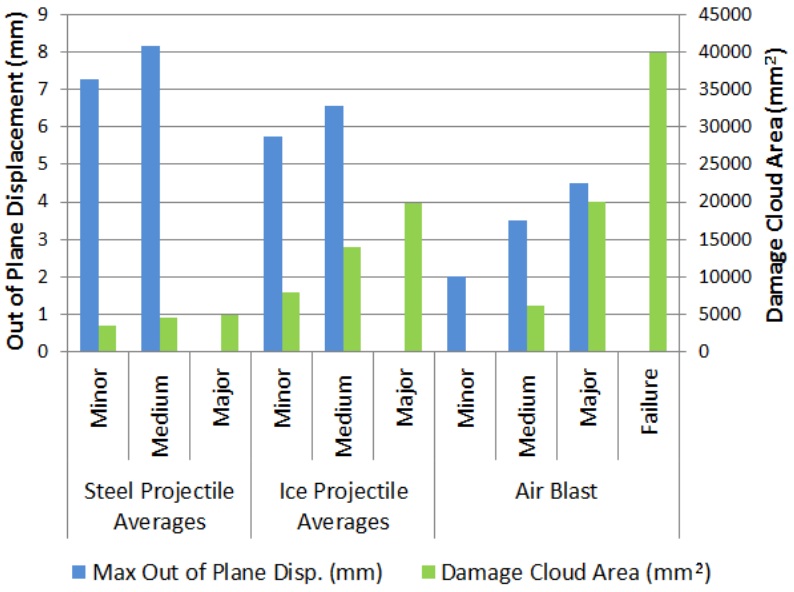

Figure 7. Maximum out-of-plane displacements and damage areas for both types of projectiles and air blast

For the case of air blast loading, the observed centre-point displacement of each specimen demonstrated changes in the oscillation period after the appearance of delamination damage (triple peaks) caused by a reduction of specimen's stiffness, not observed in the impact cases. The global deformation and transitions in curvature of each specimen remained similar as the air blast magnitude increased, whereas the out-of-plane displacement increased showing that the magnitude had no effect on the curvature and modes of oscillation during deformation for the range of air-blast magnitudes investigated. The behaviour follows a typical deformation pattern for this type of specimen fixture and size of the loading area, showing that the distributed loading led to almost instant global flexural bending, without any obvious significant localised indentation and associated damage. For the major and failure damage cases, greater deformation of the rear surface was observed at the free edges, resulting from the initiation of the tensile failure and delamination of the first few plies along the central band of damage observed.

Damage at the rear surface of the impact specimens occurred much sooner in the case of the solid projectiles; this is likely due to the almost instantaneous fragmentation of the ice projectile on impact causing a broader distribution of impact load and, therefore, a longer impact duration even at clearly higher impact energies. Although the fragmenting projectile mitigated the penetration of the specimen, the partial indentation followed by the projectile's destruction, causing delamination and removal of the first 2-3 plies from the front surface of the impacted composite plate. The resultant air-blast damage initiated and propagated from the rear surface of the specimens towards its front surface as the air blast magnitude increased, similar to that of normal three-point bending. For the minor-damage

case, no significant damage was observed, but at the major- and failure-damage cases the specimens experienced severe damage in the form of tensile failure and wide-spread delamination propagating from the central line. Given the similar global flexural bending behaviour of all the specimens across all damage cases, the initiation points of damage were consistent to their centres and free edges.

Acknowledgements
The authors are grateful to groups of Prof. Arun Shukla (University of Rhode Island, Kingston, RI, USA) and Prof. Mikhail Nikhamkin (Perm National Research Polytechnical University, Russian Federation) for implementation of experimental studies.

References

[1] Silberschmidt VV (ed.), *Dynamic Deformation, Damage and Fracture in Composite Materials and Structures*. Elsevier, Amsterdam e.a., 2016, 616 pp.
[2] Abrate S. Impact on laminated composites. *ASME: Applied Mechanics Reviews*, 44:155-190, 1991.
[3] Abrate S. Impact on laminated composites: Recent advances. Composites. *ASME: Applied Mechanics Reviews*, 47:517-544, 1994.
[4] Langdon GS, Lee WC, Louca LA. The infuence of material type on the response of plates to air-blast loading. *International Journal of Impact Engineering*, 78: 150-160, 2014.
[5] Langdon GS, Cantwel WJ, Guan ZW, Nurick GN The response of polymeric composite structures to air-blast loading: A state-of-the-art. *International Materials Reviews*, 59: 159-177, 2014.
[6] Pernas-Sánchez,. Artero-Guerrero J, Varas JA, López-Puente J. Analysis of ice impact process at high velocity. *Experimental Mechanics*, 55:1669-1679, 2015.
[7] Kim H, Welch DA, Kedward KT Experimental investigation of high velocity ice impacts on woven carbon/epoxy composite panels. *Composites Part A: Applied Science and Manufacturing*, 34:25-41, 2003.
[8] Appleby-Thomas GJ, Hazell P J, Dahini G. On the response of two commercially-important CFRP structures to multiple ice impacts. *Composite Structures*, 93:2619-2627, 2011.
[9] LeBlanc J, Shukla A, Rousseau C, Bogdanovich A. Shock loading of three-dimensional woven composite materials. *Composite Structures*, 79: 344-355, 2007.
[10] Tekalur S, Shivakumar K, Shukla A. Mechanical behavior and damage evolution in E-glass vinyl ester and carbon composites subjected to static and blast loads. *Composites Part B: Engineering*, 39: 57-65, 2008.
[11] Kumar P, Stargel DS, Shukla A. Effect of plate curvature on blast response of carbon composite panels. *Composite Structures*, 99: 19-30, 2013.
[12] Nunes LM, Paciornik S, d'Almeida JRM Evaluation of the damaged area of glass-fiber-reinforced epoxy-matrix composite materials submitted to ballistic impacts. *Composites Science and Technology*, 64: 945-954, 2004.
[13] Sevkat E. Experimental and numerical approaches for estimating ballistic limit velocities of woven composite beams. *International Journal of Impact Engineering.* 45: 16-27, 2012.
[14] Shaktivesh NS, Nair ChV, Kumar S, Naik NK. Ballistic impact performance of composite targets. *Materials & Design.* 51: 833-846, 2013.
[15] Pandya KS, Pothnis JR, Ravikumar G, Naik NK. Ballistic impact behavior of hybrid composites. *Materials & Design.* 44: 128-135, 2013.
[16] Yahaya R, Sapuan SM, Jawaid M, Leman Z, Zainudin ES. Quasi-static penetration and ballistic properties of kenaf–aramid hybrid composites. *Materials & Design*. 63: 775-782, 2014.
[17] Karthikeyan K, Russell BP, Fleck NA, Wadley HNG, Deshpande VS. The effect of shear strength on the ballistic response of laminated composite plates. *European Journal of Mechanics - A/Solids*. 42: 35-53, 2013.